Journal of Medical Imaging

MedicalImaging.SPIEDigitalLibrary.org

Compressed sensing magnetic resonance imaging based on shearlet sparsity and nonlocal total variation

Ali Pour Yazdanpanah
Emma E. Regentova

SPIE.

Ali Pour Yazdanpanah, Emma E. Regentova, "Compressed sensing magnetic resonance imaging based on shearlet sparsity and nonlocal total variation," *J. Med. Imag.* **4**(2), 026003 (2017), doi: 10.1117/1.JMI.4.2.026003.

Compressed sensing magnetic resonance imaging based on shearlet sparsity and nonlocal total variation

Ali Pour Yazdanpanah* **and Emma E. Regentova**
University of Nevada, Electrical and Computer Engineering Department, Las Vegas, Nevada, United States

Abstract. Compressed sensing (CS) has been utilized for acceleration of data acquisition in magnetic resonance imaging (MRI). MR images can then be reconstructed with an undersampling rate significantly lower than that required by the Nyquist sampling criterion. However, the CS usually produces images with artifacts, especially at high reduction rates. We propose a CS MRI method called shearlet sparsity and nonlocal total variation (SS-NLTV) that exploits SS-NLTV regularization. The shearlet transform is an optimal sparsifying transform with excellent directional sensitivity compared with that by wavelet transform. The NLTV, on the other hand, extends the TV regularizer to a nonlocal variant that can preserve both textures and structures and produce sharper images. We have explored an approach of combining alternating direction method of multipliers (ADMM), splitting variables technique, and adaptive weighting to solve the formulated optimization problem. The proposed SS-NLTV method is evaluated experimentally and compared with the previously reported high-performance methods. Results demonstrate a significant improvement of compressed MR image reconstruction on four medical MRI datasets. [DOI: 10.1117/1.JMI.4.2.026003]

Keywords: compressed sensing; magnetic resonance imaging; shearlet sparsity; nonlocal total variation.

Paper 16268RR received Dec. 16, 2016; accepted for publication Jun. 7, 2017; published online Jun. 28, 2017.

1 Introduction

Compressed sensing (CS)[1–3] is a way of speeding the signal acquisition by providing means for smarter sampling. Since 2006, compressed sensing or compressive sampling has been receiving considerable attention in theory and applications, and, among them, magnetic resonance imaging (MRI) is one whose implied sparsity suggested the use of sparse sampling. Compared with the standard sampling theory, MR images are speed-limited physically and constrained by physiological nature.[4] Acceleration of MRI while preserving image quality has a major impact in diagnostics. Such acceleration may be provided by exploiting MRI sparsity by means of undersampling and efficient image reconstruction, which are the main goals of CS.[1,5]

CS allows the recovery of magnetic resonance images from vastly undersampled k-space data without being constrained by Shannon/Nyquist requirements.[2] The process includes encoding, sensing, and decoding processes. Most of the compressed MRI approaches are based on the linear model $Ax = b, A = SF$, where S is a selection or a sampling matrix, F is a two-dimensional (2-D) discrete Fourier matrix, and b is the observed k-space data, which are significantly undersampled, that is beyond the limits of the fundamental sampling theorem. Given the sparsity assumption about $\hat{x}$ which is an estimate of x, where x is the image, one possible solution would be $\{\min_x |x|_0 : Ax = b\}$, but, since solving ℓ_o-minimization problem is NP-hard,[6] a reasonable alternative would be $\{\min_x |x|_1 : Ax = b\}$. $|.|_0$ denotes ℓ_0-norm. Thus, the objective is to minimize absolute differences (variation), and it is useful to penalize by finite differences. For this reason, TV is used for checking the sparsity by forming finite differences and coarse denoising.

The review of the CS MRI methods shows how to solve the above problem with different regularization and penalty terms. For example, He et al.[7] proposed a model for compressed MRI using two nonsmooth regularization terms to attain accuracies superior to the total variation (TV) regularization model.[8] Chang et al.[9] proposed a partial differential equation-based method to reconstruct MR images. Lysaker et al.[10] improved the quality of reconstructed images by introducing a fourth-order regularization term yielding the MRI model too complex to solve for high-resolution images. Lustig et al.[4] reviewed different compressed MRI steps and developed a model using sparsity of the wavelets and exploiting ℓ_1-minimization to reconstruct the MR image. Jung et al.,[11] Ye et al.,[12] Candes et al.,[13] and Chartrand and Yin,[14] explored ℓ_p-quasinorm minimization model $0 < p < 1$ using FOCUSS[15] to reconstruct MR images, but, because of nonconvexity of the objective function, a global minima was not guaranteed. Trzasko et al.[16] proposed a homotopic nonconvex objective function based on the ℓ_0-minimization model; however, it has the global minima issue.

Recent CS efforts in MR pursue a best combination of sparsifying transforms[17–22] and a fast solution toward obtaining a high-quality reconstruction. Various methods have been presented to reconstruct MR images from undersampled data. Ma et al.[17] introduced an operator-splitting algorithm, total variation compressed MR imaging (TVCMRI) for MR image reconstruction. Knoll et al.[18] presented total generalized variation for MRI reconstruction. By taking advantage of fast wavelet and Fourier transforms, TVCMRI can process actual MR data accurately. Yang et al.[19] solved the same objective function presented in Ref. 17 by a variable splitting method [reconstruction from partial Fourier data (RecPF)], which is TV-based $\ell_1 - \ell_2$ MR reconstruction. This method uses an alternating direction method for

*Address all correspondence to: Ali Pour Yazdanpanah, E-mail: pouryazd@unlv.nevada.edu

2329-4302/2017/$25.00

recovering MR images from incomplete Fourier measurements and solving it as in Ref. 20. A fast composite splitting algorithm (FCSA)[21] was proposed by Huang et al. FCSA is based on the combination of variable and operator splitting. It splits the variable x into two variables and exploits the operator-splitting method to minimize the regularization terms over the splitting variables.

Nonlocal total variation for MR reconstruction (NTVMR)[22] and the framelet + nonlocal TV (FNTV)[23] methods have been proposed lately. In Ref. 24, the use of the first-order derivatives is analyzed to have two major shortcomings, such as oil-painting artifacts and contrast loss. Out of the two methods that use nonlocal TV regularization, FNTV delivers a better quality. FNTV is formulated to minimize the combination of nonlocal TV, framelet, and the least-square data fitting terms. Recently, shearlet-based methods have been proposed for MR reconstruction purposes.[25,26] A new framework, i.e., "nonseparable shearlet transform iterative soft thresholding reconstruction algorithm" (FNSISTRA), was presented by Pejoski et al.[26] Along with the discrete nonseparable shearlet transform[27] as a sparsifying transform, the authors used a fast-iterative soft thresholding algorithm[28,29] to solve their reconstruction formulation. In Ref. 30, an MRI reconstruction method (BM3D-MRI) that utilized decoupled iterations alternating over a BM3D denoising step algorithm and a reconstruction step was presented. The method, in most cases, has accomplished the reconstruction with a better signal-to-noise ratio (SNR) measured than those by the abovementioned state-of-the-art methods, where $\mathrm{SNR} = 10\log_{10}\frac{\|x\|_2^2}{\|x-x^n\|_2^2}$, x is the original image, and x^n represents the reconstructed image after n iterations.

In this paper, we propose an optimization scheme for MR image reconstruction. It integrates the SS-NLTV. Sparsifying transforms such as wavelets are not always able to handle edges or curves, and, in general, singularities in higher dimensions. Shearlets are efficient in representing anisotropic features that comprise the object shape and express textures such as edges of various orientations, strengths, and scales, and thus their inclusion into regularization promises a better performance compared with those by wavelets, which are isotropic objects. On the other hand, the NLTV, which is the TV extension to a nonlocal variant, preserves fine structures, details, and textures and prevents the oil-painting artifacts inherent to TV, while maintaining the contrast.

The goal of obtaining a higher quality of reconstruction than that demonstrated by advanced methods such as TVCMRI,[17] RecPF,[19] FCSA,[21] FNTV,[23] FNSISTRA,[26] and BM3D-MRI[30] is attained as confirmed by the experimental study.

The rest of the paper is organized as follows: the SS-NLTV method is described in Sec. 2, the results and performance comparison are presented in Sec. 3, and the conclusions are drawn in Sec. 4.

2 Shearlet Sparsity-Nonlocal Total Variation Method

The MRI model can be expressed as

$$Ax = b, \tag{1}$$

where $x \in \mathbb{R}^M$ is an MR image, $A \in \mathbb{R}^{N\times M}$ is a measurement matrix with $N \ll M$, and $b \in \mathbb{R}^N$ is the observed data. The MR data can be recovered by solving the following minimization problem:

$$\text{minimize } J(x) \quad \text{subject to } Ax = b, \tag{2}$$

$$\text{when } J(x) = |\Phi(x)|_1, \tag{3}$$

where $J(x)$ is a regularizing functional and Φ is a sparsifying transform. In the CS model of MRI, $A = SF$, where S is a selection or a sampling matrix, F is the 2-D discrete Fourier matrix, and b is the observed k-space data. Assuming the sparsity of the model, the problem is ill-posed for minimizing the least-squares function. Therefore, the following cost function with a regularization term has been considered:

$$\min_x |\Phi(x)|_1 \quad \text{subject to } \|Ax-b\|_2^2 \le \sigma, \tag{4}$$

where σ is the variance of distortion in b. In Eq. (4), $|.|_1$ denotes ℓ_1-norm and $\|.\|_2$ denotes ℓ_2-norm. The constrained optimization in Eq. (3) is equivalent to the following unconstrained optimization problem as it is formulated in Ref. 13:

$$\min_x |\Phi(x)|_1 + \frac{\lambda}{2}\|Ax-b\|_2^2, \tag{5}$$

where $\lambda > 0$ is a balancing constant, which relies on the sparsity of the underlying MR image x under linear transformation.

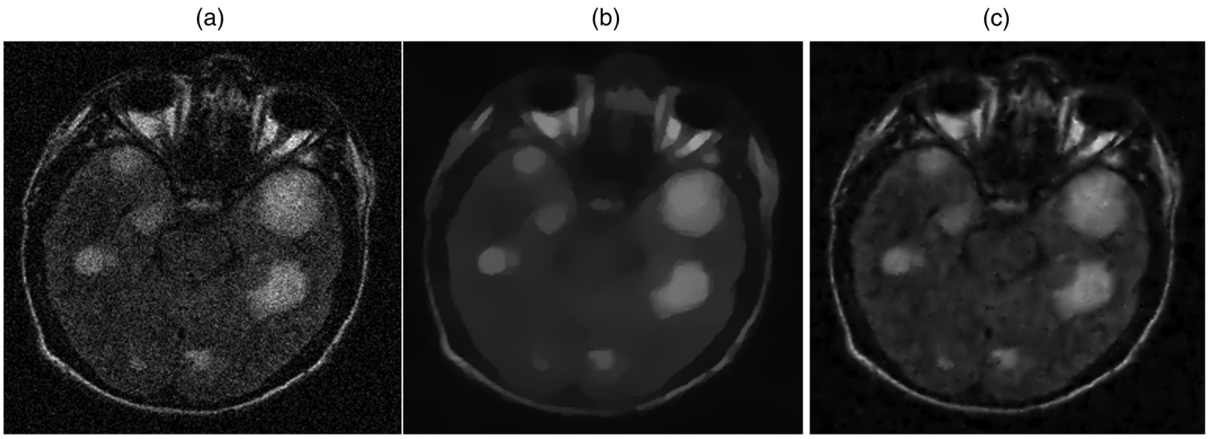

Fig. 1 (a) Noisy MRI image, radial subsampling under 20% rate, (b) recovered using TV, and (c) recovered using NLTV.

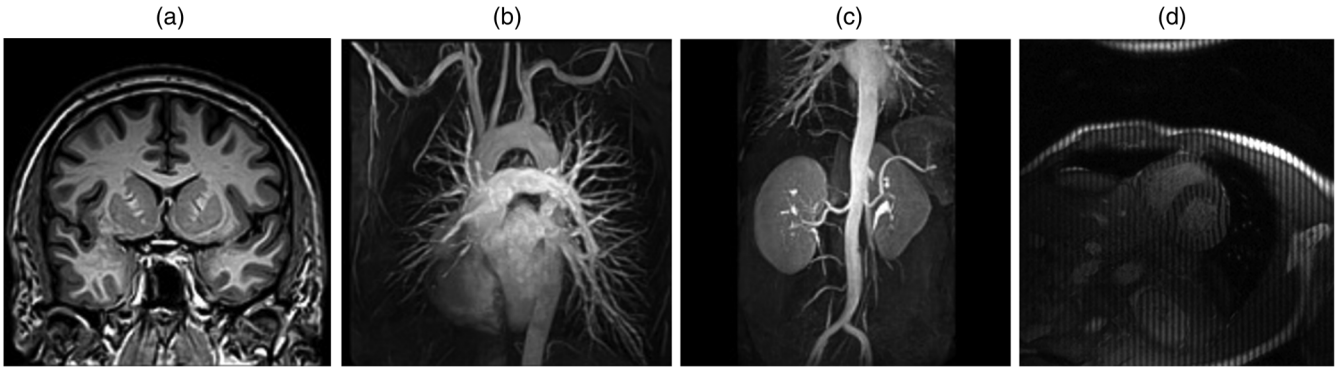

Fig. 2 Images used to test the performance of the proposed CT-TGV method and for comparison: (a) brain, (b) chest, (c) artery, and (d) cardiac.

Also, λ can be interpreted as a contribution of the regularization to the total cost. The lower its value is, the less is the importance of the data fitting term, which amounts to more regularization. λ remains constant across the iterations; therefore, we choose a value for λ that minimizes the condition number of the subproblems. We have determined that when $\lambda = 10$, the convergence is reached with a fewer number of iterations.

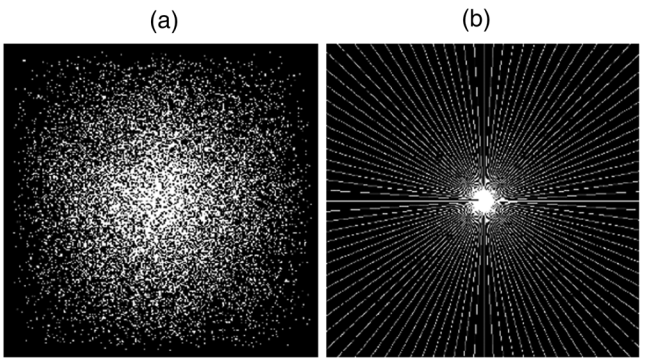

Fig. 3 (a) Random variable subsampling and (b) radial subsampling.

Considering the problem, we propose and formulate the optimization problem using a combination of both the NLTV and the shearlet as regularizers. The proposed optimization problem to obtain reconstruction $\hat{x}$ is as follows:

$$\hat{x} = \text{argmin}_x \alpha |\nabla_w x|_1 + \beta \sum_k |SH_k(x)|_1 + \frac{\lambda}{2} \|Ax - \|_2^2, \quad (6)$$

where $|\nabla_w x|_1 = \sum_t |\nabla_w x_t|_1$ is the NLTV norm and nonlocal weights w are computed from image estimate $\hat{x}$. $SH(x)$ is the combination of different subbands of shearlet transform. $0 < \alpha < 1$ and $0 < \beta < 1$ are the weighting parameters stressing two regularization terms. The values of these two parameters in each loop are adaptively derived based on the variance of noise present in the reconstructed image from a previous iteration. We stress more on the shearlet regularizer term if the estimated variance in each shearlet subband is greater than a specified threshold. The variances of the signal in every shearlet subband are computed by exploiting the maximum likelihood estimator applied on the neighborhood (a square) areas of coefficients.

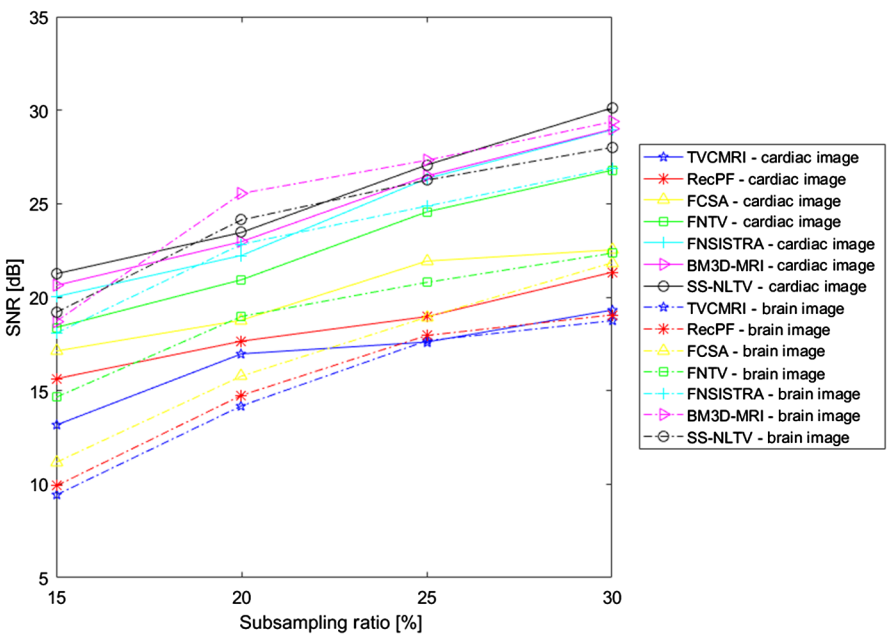

Fig. 4 Performance of methods with random variable density subsampling for cardiac and brain images.

2.1 *Nonlocal Total Variation*

NLTV is defined to describe the patch-level correspondence in contrast to the TV, which is based on the correspondence at the pixel level.[31] For image x, the nonlocal weights can be formed concerning any two spatial nodes i and j,

$$\varpi_x(i,j) = e^{-\frac{\int_{\mathcal{R}_1} G_\sigma(t)[x(j+t)-x(i+t)]^2 dt}{\sigma^2}}, \tag{7}$$

where G is a Gaussian kernel with the variance σ^2 and $\mathcal{R}_1$ characterizes the spatial neighborhood around i and j for similarity consideration. The nonlocal gradient $\nabla_w x(i,j)$ at i is described as a vector of all partial derivatives $\nabla_w x(i,.)$[32]

$$\nabla_w x(i,j) = [x(j) - x(i)] \sqrt{\varpi_x(i,j)}, \quad \forall\ j \in \mathcal{R}_2, \tag{8}$$

where $\mathcal{R}_2$ is the spatial neighborhood around i, whose nonlocal gradient $\nabla_w x(i,j)$ is calculated. The adjoint of Eq. (8) is derived from the adjoint relationship with a nonlocal divergence operator div_w as

$$\langle \nabla_w x, v \rangle = \langle x, \mathrm{div}_w v \rangle, \tag{9}$$

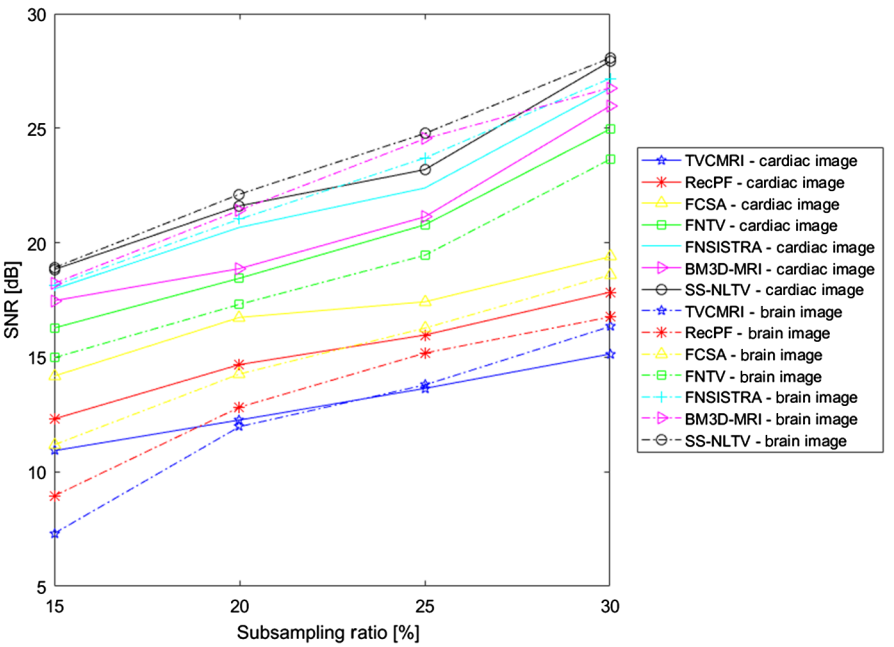

Fig. 5 Performance of methods with radial subsampling for cardiac and brain images.

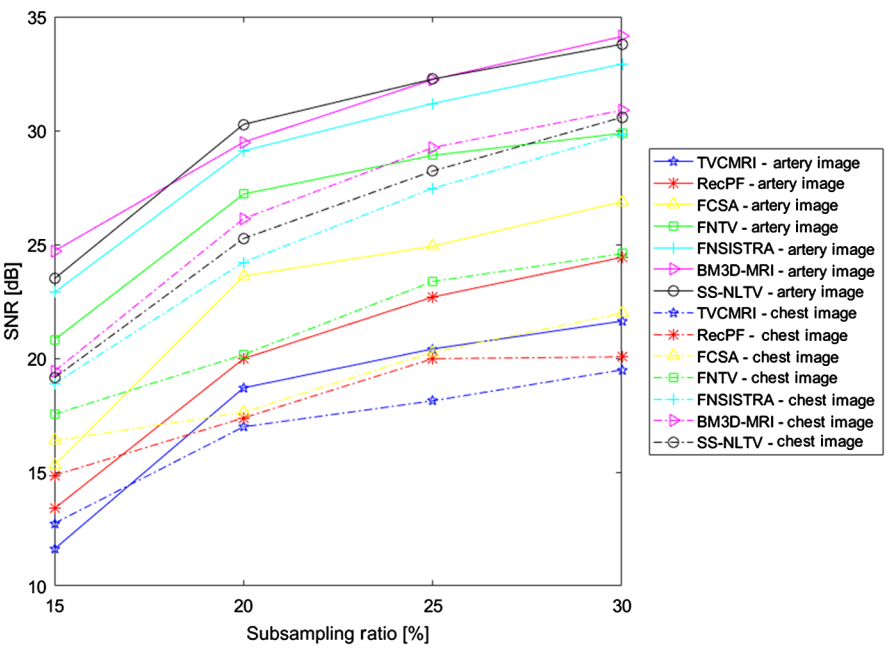

Fig. 6 Performance of methods with random variable density subsampling for artery and chest images.

$$\mathrm{div}_w v(i,j) = \int_{\mathcal{R}_2} [v(i,j) - v(j,i)]\sqrt{\varpi_x(i,j)}\mathrm{d}j. \tag{10}$$

For image $x \in \mathbb{R}^M = \mathbb{R}^{m\times n}$ and $\mathcal{R}_1 = \mathbb{R}^{(2a_1+1)(2b_1+1)}$ and $\mathcal{R}_2 = \mathbb{R}^{(2a_2+1)(2b_2+1)}$, weights in Eq. (8) are calculated according to Eq. (11)

$$\varpi_x(k_1,l_1,k_2,l_2) = e^{-\frac{\sum_{z_1=0}^{2a_1}\sum_{z_2=0}^{2b_1} G_\sigma(z_1,z_2)[x(k_1-a_1+z_1,l_1-b_1+z_2)-x(k_2-a_1+z_1,l_2-b_1+z_2)]^2}{\sigma^2}} \quad k_1,k_2 = 1,\ldots,m.\ l_1,l_2 = 1,\ldots,n, \tag{11}$$

and nonlocal gradient $\nabla_w x \in \mathbb{R}^{m\times n\times(2a_2+1)\times(2b_2+1)}$ can be calculated as

$$\nabla_w x(k_1,l_1,:,:) = \begin{bmatrix} [x(k_1-a_2,l_1-b_2)-x(k_1,l_1)]\sqrt{\varpi_x(k_1-a_2,l_1-b_2,k_1,l_1)} & \cdots & [x(k_1-a_2,l_1+b_2)-x(k_1,l_1)]\sqrt{\varpi_x(k_1-a_2,l_1+b_2,k_1,l_1)} \\ [x(k_1-a_2+1,l_1-b_2)-x(k_1,l_1)]\sqrt{\varpi_x(k_1-a_2+1,l_1-b_2,k_1,l_1)} & \cdots & [x(k_1-a_2+1,l_1+b_2)-x(k_1,l_1)]\sqrt{\varpi_x(k_1-a_2+1,l_1+b_2,k_1,l_1)} \\ \cdots & \cdots & \cdots \\ [x(k_1+a_2,l_1-b_2)-x(k_1,l_1)]\sqrt{\varpi_x(k_1+a_2,l_1-b_2,k_1,l_1)} & \cdots & [x(k_1+a_2,l_1+b_2)-x(k_1,l_1)]\sqrt{\varpi_x(k_1+a_2,l_1+b_2,k_1,l_1)} \end{bmatrix}, \tag{12}$$

where $\nabla_w x(k_1,l_1,:,:)$ is a 2-D submatrix acquired by stacking the third and fourth dimensions of $\nabla_w x$ at the k_1'th location in the first and the l_1'th location in the second dimension. $a_1 = b_1 = 3$ and $a_2 = b_2 = 5$ in $\mathcal{R}_1$ and $\mathcal{R}_2$ neighborhoods, respectively. Figure 1 shows the comparison of TV versus NLTV reconstruction from a noisy MRI image.

2.2 *Shearlet Sparsity*

Shearlet transform is introduced and investigated in Refs. 33–37 and generally has been used for solving the inverse problems.[38,39] Let $\psi_{a,s,t}$ denote the shearlet basis functions or simply shearlets. The continuous shearlet transformation of image f is defined as

$$SH_{a,s,t}(x) = \int_{\mathcal{R}^2} f(x)\psi_{a,s,t}(t-x)\mathrm{d}x, \tag{13}$$

where $s \in \mathcal{R}$, $a \in \mathcal{R}$, and $t \in \mathcal{R}^2$ define the orientation, scale, and location in the spatial domain, respectively, and $f(x) \in \mathcal{R}^2$ is a 2-D reconstructed image. Shearlets are shaped by dilating, shearing, and translating the mother shearlet $\psi_{a,s,t} \in \mathcal{R}^2$, as follows:

$$\psi_{a,s,t}(x) = |\det(K_{a,s})|^{-\frac{1}{2}}\psi[K_{a,s}^{-1}(x-t)], \tag{14}$$

$$K_{a,s} = \begin{pmatrix} a & \sqrt{a}s \\ 0 & \sqrt{a} \end{pmatrix} = BS = \begin{pmatrix} 1 & s \\ 0 & 1 \end{pmatrix}\begin{pmatrix} a & 0 \\ 0 & \sqrt{a} \end{pmatrix}, \tag{15}$$

where S is an anisotropic scaling matrix with a scaling parameter $a > 0$ and B is a shear matrix with a factor $s \in \mathcal{R}$. B and S are both invertible matrices, with $\det(B) = 1$. $\det(A)$ is the determinant of matrix A. The shearlet mother function ψ is a composite wavelet, which fulfills admissibility conditions.[38,40] The Meyer

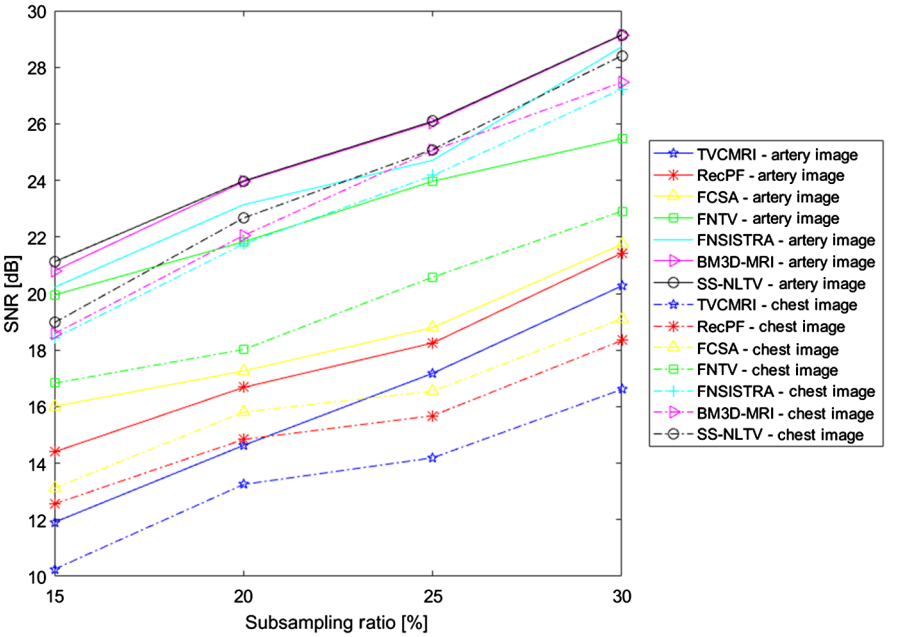

Fig. 7 Performance of methods with radial subsampling for artery and chest images.

wavelet with a good localization ability in both time and frequency spaces is exploited as a mother wavelet for ψ in the shearlet transformation. In addition to its localization properties, Meyer wavelet filters are directly described in the frequency space by $\Psi(\omega)=\Psi_1(\omega_1)\Psi_2(\omega_2/\omega_1)$ with $\omega=[\omega_1,\omega_2]$, $\Psi_1(\omega_1)$ being the Fourier transform of the wavelet function (ψ) and $\Psi_2(\omega_2)$ being a compactly supported bump function $\Psi_2(\omega_2)=0\leftrightarrow\omega_2\notin[-1,1]$.[41,42] The shearlet transform is invertible if the function ψ satisfies the admissibility property

$$\iint_{\mathbb{R}^2}\frac{|\Psi(\omega_1,\omega_2)|^2}{|\omega_1|^2}\mathrm{d}\omega_1\mathrm{d}\omega_2<\infty. \tag{16}$$

Assume l is a function describing piecewise smooth functions with discontinuities along C^2 curves, and l_{SH_p} is the shearlet approximation of l obtained by taking the p largest absolute shearlet coefficients, then

$$\|l-l_{SH_p}\|_2\leq Cp^{-2}(\log\ p)^3, \tag{17}$$

as $p\to\infty$, while the asymptotic error is Cp^{-1} for wavelet. Therefore, shearlet transform is better in sparsely approximating piecewise smooth images. We can implement the k'th subband of the shearlet transform (SH_k) as a mask Z_k in the frequency domain[43]

$$SH_k(x)=F^*\mathrm{diag}[\mathrm{vec}(Z_k)]F\cdot x=P_k\cdot x, \tag{18}$$

where vec is the vectorizing ($R^{n\times n}\to R^{n^2}$) and diag is the matricization diagonal ($R^n\to R^{n\times n}$) operators.

2.3 *Solution*

The optimization problem is formulated as follows:

$$\mathrm{argmin}_x\alpha|\nabla_w x|_1+\beta\sum_k|SH_k(x)|_1+\frac{\lambda}{2}\|Ax-b\|_2^2. \tag{19}$$

The problem has both l_1- and l_2-norm terms, and, thus, the solution in a closed-form is difficult to obtain. The alternating direction method of multiplier (ADMM)[44] and splitting variables are used to solve the formulated problem as follows:

$$\mathrm{argmin}_x\alpha|y_1|_1+\beta\sum_k|y_2(k)|_1+\frac{\lambda}{2}\|Ax-b\|_2^2$$
$$\text{subject to } y_1=\nabla_w x, y_2(k)=SH_k(x), \tag{20}$$

where $y_1\in\mathbb{R}^M$ and $y_2(k)\in\mathbb{R}^M$ are the auxiliary variables.

The split Bregman method,[45] as a technique for solving a variety of ℓ_1-regularized, is another reinterpretation of the ADMM method. We have also solved our problem with split Bregman, but since we choose the regularization parameters adaptively, we were able to reach faster convergence with ADMM compared with that of split Bregman, and this is the reason we have chosen ADMM as part of the solution.

The Lagrangian function for the problem in Eq. (20) can be written as follows:

$$\mathcal{L}(x,y_1,y_2,u_1,u_2)=\frac{\lambda}{2}\|Ax-b\|_2^2+\alpha|y_1|_1$$
$$+\frac{\eta}{2}\|\nabla_w x-y_1+u_1\|_2^2+\beta\sum_k|y_2(k)|_1$$
$$+\frac{\Gamma}{2}\sum_k\|SH_k(x)-y_2(k)+u_2(k)\|_2^2, \tag{21}$$

where $u_1\in\mathbb{R}^M$ and $u_2(k)\in\mathbb{R}^M$ are the newly defined scaled dual variables.

Finally, the problem is solved by iterating over Eqs. (22)–(26)

$$x^{(n+1)}=\mathrm{argmin}_x\mathcal{L}[x,y_1^{(n)},y_2^{(n)},u_1^{(n)},u_2^{(n)}], \tag{22}$$

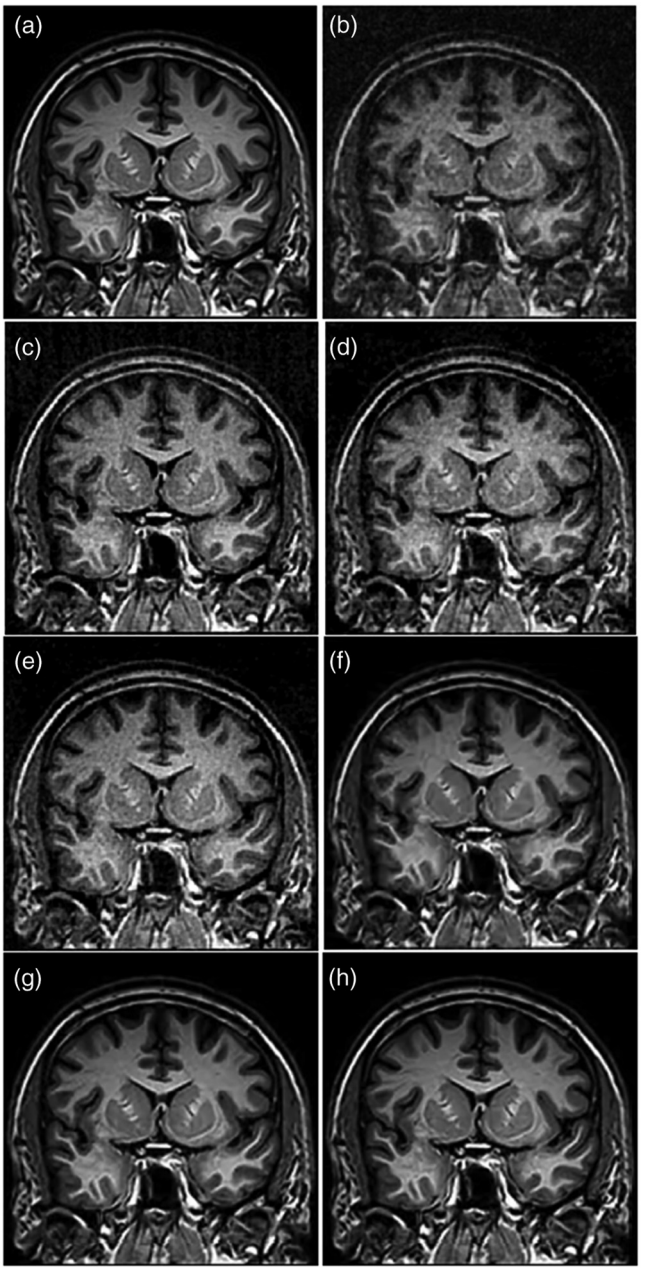

Fig. 8 Reconstruction of brain image from 20% radial subsampling: (a) original, (b) TVCMRI, (c) RecPF, (d) FCSA, (e) FNTV, (f) FNSISTRA, (g) BM3D-MRI, and (h) SS-NLTV.

$$y_1^{(n+1)} = \text{argmin}_{y_1}\mathcal{L}[x^{(n+1)}, y_1, u_1^{(n)}], \tag{23}$$

$$y_2^{(n+1)} = \text{argmin}_{y_2}\mathcal{L}[x^{(n+1)}, y_2, u_2^{(n)}], \tag{24}$$

$$u_1^{(n+1)} = u_1^{(n)} + [\nabla_w x^{(n+1)} - y_1^{(n+1)}], \tag{25}$$

$$u_2^{(n+1)} = u_2^{(n)} + \{SH[\mathrm{x}^{(n+1)}] - y_2^{(n+1)}\}. \tag{26}$$

The optimal solution for the subproblem by Eq. (22) requires finding roots of its derivatives, which leads to Eq. (27)

$$\lambda A^{\mathrm{T}}Ax - \lambda A^{\mathrm{T}}b + \eta\,\text{div}_w(\nabla_w x - y_1 + u_1) + \Gamma\{\sum_k P_k^* P_k \mathrm{x} + \sum_k P_k^*[y_2(k) - u_2(k)]\} = 0, \tag{27}$$

where we can solve it in the Fourier domain by multiplying both sides of it by F

$$\{\lambda S + \eta F\text{div}_{\mathrm{w}}\nabla_w F^* + \Gamma\sum_k \text{diag}[\text{vec}(|Z_k|^2)]\}$$
$$Fx = \lambda b + \eta F\text{div}_w(y_1 - u_1) + \Gamma\sum_k \text{diag}[\text{vec}(Z_k)]F[u_2(k) - y_2(k)]. \tag{28}$$

Minimization in Eqs. (23) and (24) can be attained by shrinkage operators such as[45]

$$y_1^{(n+1)} \coloneqq \text{Shrink}[\nabla_w x^{(n+1)} + u_1^{(n)}, \vartheta_2], \tag{29}$$

$$y_2^{(n+1)} \coloneqq \text{Shrink}\{SH[\mathrm{x}^{(n+1)}] + u_2^{(n)}, \vartheta_2\}, \tag{30}$$

where $\vartheta_1 = \frac{\alpha}{\eta}$, $\vartheta_2 = \frac{\beta}{\Gamma}$, and

$$\text{Shrink}(x, \xi)_n = \text{sign}(x_n).\max\{|x_n| - \xi, 0\}. \tag{31}$$

3 Results

We test the proposed SS-NLTV method on four 256×256 MR images, i.e., brain, chest, artery, and cardiac images,[19] as shown in Fig. 2. The cardiac image is intentionally used as a test image to demonstrate the reconstruction of an image with artifacts. The input data in our experiments include only the magnitude values. Six high-performance methods are chosen for comparison, i.e., TVCMRI,[17] RecPF,[19] FCSA,[21] FNTV,[23] FNSISTRA,[26] and BM3D-MRI.[30] For realization of the method, we used shearlab[46] to obtain shearlet coefficients because of the fast implementation. The methods are studied with two subsampling techniques, i.e., random variable subsampling and radial subsampling. Figure 3 visualizes these two types of subsampling. We demonstrate results for the fixed number of 50 iterations as the methods under comparison utilized this number as a stopping point to reach the convergence. Four sampling ratios to acquire the measurement b are 15%, 20%, 25%, and 30%. Figures 4–7 show SNR plots for methods under comparison, where $\text{SNR} = 10\log_{10}\frac{\|x\|_2^2}{\|x-x^n\|_2^2}$, x is the original image, and x^n represents the reconstructed image after n interations. SNR values are measured for the above quantities of subsampling ratios, with radial and random subsampling.

Our method outperforms the BM3D-MRI in the radial subsampling experiments (for brain, cardiac, and artery MR images). Also, our method shows a better performance with a large margin on the cardiac image with the stripe pattern artifact. The BM3D-MRI method achieves a better performance in the random subsampling experiments on three MR images but lacks the performance with the cardiac image when the random

Table 1 The SNRs (db) by all the methods at 20% random and radial subsampling ratios.

Method	Brain		Cardiac		Chest		Artery	
Subsampling	Radial	Random	Radial	Random	Radial	Random	Radial	Random
TVCMRI	11.97	14.19	12.26	16.97	13.25	16.99	14.63	18.70
RecPF	12.82	14.75	14.68	17.65	14.84	17.38	16.68	19.98
FCSA	14.27	15.78	16.74	18.77	15.81	17.63	17.26	23.61
FNTV	17.31	18.97	18.45	20.93	18.02	20.16	21.83	27.21
FNSISTRA	21.03	22.83	20.67	22.23	21.75	24.22	23.14	29.11
BM3D-MRI	21.42	**25.55**	18.87	22.97	**23.05**	**26.13**	23.95	29.49
SS-NLTV	**22.12**	24.13	**21.61**	**23.46**	22.67	25.26	**23.98**	**30.27**

Note: The bold value shows the maximum SNR value for each column (each image with specific subsampling) in the table.

Table 2 Run times for different methods.

Method	TVCMRI	RecPF	FCSA	FNTV	FNSISTRA	BM3D-MRI	SS-NLTV
Time (s)	1.1419	0.9157	0.6499	5.2785	9.8147	21.9058	7.1270

subsampling is used. The results can be explained by the fact that the BM3D-MRI uses a powerful denoiser, which copes very well with random noise. The success of our method on radial sampling is secured by directional selectivity of shearlets. We demonstrate the reconstruction results for brain image with radial subsampling in Fig. 8. Table 1 shows the SNRs (db) by all the methods at 20% random and radial subsampling ratios.

The superior performance of SS-NLTV is derived from utilization of NLTV, which locates sharper edges and suppresses artifacts; it is due to the exceptional spatial localization and directional selectivity of the shearlet transform. Table 2 shows the run times calculated for all the methods under comparison (for brain image and 20% random subsampling). All the implementations of different algorithms were run on 4 Gigabyte RAM, Intel core 2 Duo E8400 processor, and with the NVIDIA Tesla C2050 GPU board. The execution times of the implementations are average values over five executions.

4 Conclusion

In this paper, we have presented a method, the SS-NLTV for compressively sampled MRI reconstruction. The method utilizes sparsifying shearlet transform and the NLTV in collaboration to gain on directional sensitivity and selective regularization at different levels of transformation. We formulated the optimization problem for the reconstruction process and solved it uniquely by combining ADMM, splitting variables technique, and adaptive weighting. The method is aimed at reconstructing images with a high quality assessed visually and using objective quality metrics. Specifically, oil-painted artifacts common for CS and specifically pronounced at high reduction factors have not been observed in reconstructed images. High SNRs produced by the method quantify its high performance. The conducted experiments and the analysis of different reconstructed medical MRI datasets under different types of subsampling and ratios have demonstrated a superior quality of reconstruction by the proposed method in comparison with six reference methods, including the state-of-the-art BM3D-MRI method.

Disclosures

No conflicts of interest, financial or otherwise, are declared by the authors.

Acknowledgments

The authors would like to thank NASA EPSCoR for the financial support through cooperative Agreement No. NNX10AR89A for this research work. This article does not contain any studies with human participants or animals performed by any of the authors.

References

1. E. J. Candès, J. Romberg, and T. Tao, "Robust uncertainty principles: exact signal reconstruction from highly incomplete frequency information," *IEEE Trans. Inf. Theory* **52**(2), 489–509 (2006).
2. D. L. Donoho, "Compressed sensing," *IEEE Trans. Inf. Theory* **52**(4), 1289–1306 (2006).
3. E. J. Candès, J. K. Romberg, and T. Tao, "Stable signal recovery from incomplete and inaccurate measurements," *Commun. Pure Appl. Math.* **59**, 1207–1223 (2006).
4. M. Lustig, D. Donoho, and J. M. Pauly, "Sparse MRI: the application of compressed sensing for rapid MR imaging," *Magn. Reson. Med.* **58**(6), 1182–1195 (2007).
5. M. Lustig et al., "A look at how CS can improve on current imaging techniques," *IEEE Signal Process. Mag.* **25**(2), 72–82 (2008).
6. B. K. Natarajan, "Sparse approximate solutions to linear systems," *SIAM J. Comput.* **24**, 227–234 (1995).
7. L. He et al., "MR image reconstruction by using the iterative refinement method and nonlinear inverse scale space methods," UCLA CAM Report 06-35 (2006).
8. K. T. Block, M. Uecker, and J. Frahm, "Undersampled radial MRI with multiple coils. Iterative image reconstruction using a total variation constraint," *Magn. Reson. Med.* **57**(6), 1086–1098 (2007).
9. T.-C. Chang, L. He, and T. Fang, "MR image reconstruction from sparse radial samples using Bregman iteration," in *Proc. of the 13th Annual Meeting of ISMRM*, Seattle, p. 696 (2006).
10. M. Lysaker, A. Lundervold, and X. C. Tai, "Noise removal using fourth-order partial differential equations with applications to medical magnetic resonance images in space and time," *IEEE Trans. Image Process.* **12**, 1579–1590 (2002).
11. H. Jung, J. Ye, and E. Kim, "Improved k-t blask and k-t sense using FOCUSS," *Phys. Med. Biol.* **52**, 3201–3226 (2007).
12. J. C. Ye et al., "Projection reconstruction MR imaging using FOCUSS," *Magn. Reson. Med.* **57**(4), 764–775 (2007).
13. E. Candes, M. Wakin, and S. Boyd, "Enhancing sparsity by reweighted l_1 minimization," *J. Fourier Anal. Appl.* **14**(5), 877–905 (2008).
14. R. Chartrand and W. Yin, "Iteratively reweighted algorithms for compressive sensing," in *IEEE Int. Conf. on Acoustics, Speech and Signal Processing*, pp. 3869–3872 (2008).
15. B. D. Rao and K. Kreutz-Delgado, "An affine scaling methodology for best basis selection," *IEEE Trans. Signal Process.* **47**, 187–200 (1999).
16. J. Trzasko, A. Manduca, and E. Borisch, "Highly undersampled magnetic resonance image reconstruction via homotopic l0-minimization," in *Workshop on Statistical Signal Processing (SSP 2007)* (2007).
17. S. Ma et al., "An efficient algorithm for compressed MR imaging using total variation and wavelets," in *Proc. of Computer Vision and Pattern Recognition* (2008).
18. F. Knoll et al., "Second order total generalized variation (TGV) for MRI," *Magn. Reson. Med.* **65**(2), 480–491 (2011).
19. J. Huang, S. Zhang, and D. Metaxas, "Efficient MR image reconstruction for compressed MR imaging," *Med. Image Anal.* **15**(5), 670–679 (2011).
20. J. Yang, Y. Zhang, and W. Yin, "A fast alternating direction method for TVL1-L2 signal reconstruction from partial Fourier data," *IEEE J. Sel. Top. Signal Process.* **4**(2), 288–297 (2010).
21. D. Gabay and B. Mercier, "A dual algorithm for the solution of nonlinear variational problems via finite-element approximations," *Comput. Math. Appl.* **2**, 17–40 (1976).
22. V. P. Gopi et al., "MR image reconstruction based on iterative split Bregman algorithm and non-local total variation," *J. Comput. Math. Method Med.* **2013**, 1–16 (2013).
23. V. P. Gopi et al., "MR image reconstruction based on framelets and nonlocal total variation using split Bregman method," *Int. J. CARS* **9**, 459–472 (2014).
24. S. Osher et al., "An iterative regularization method for total variation-based image restoration," *Multiscale Model Simul.* **4**, 460–489 (2005).
25. W. Guo, J. Qin, and W. Yin, "A new detail-preserving regularity scheme," *SIAM J. Imaging Sci.* **7**(2), 1309–1334 (2014).
26. S. Pejoski, V. Kafedziski, and D. Gleich, "Compressed sensing MRI using discrete nonseparable Shearlet transform and FISTA," *IEEE Signal Process. Lett.* **22**(10), 1566–1570 (2015).
27. W.-Q. Lim, "Nonseparable shearlet transform," *IEEE Trans. Image Process.* **22**(5), 2056–2065 (2013).
28. A. Beck and M. Teboulle, "A fast iterative shrinkage-thresholding algorithm for linear inverse problems," *SIAM J. Imaging Sci.* **2**(1), 183–202 (2009).
29. W. Hao et al., "Fast iterative contourlet thresholding for compressed sensing MRI," *Electron. Lett.* **49**(19), 1206–1208 (2013).
30. E. M. Eksioglu, "Decoupled algorithm for MRI reconstruction using nonlocal block matching model: BM3D-MRI," *J. Math. Imaging Vision* **56**(3), 430–440 (2016).
31. A. Buades, B. Coll, and J. M. Morel, "A review of image denoising algorithms, with a new one," *Multiscale Model. Simul.* **4**, 490–530 (2005).
32. G. Gilboa and S. Osher, "Nonlocal operators with applications to image processing," *Multiscale Model. Simul.* **7**, 1005–1028 (2008).

33. K. Guo and D. Labate, "Optimally sparse multidimensional representation using shearlets," *SIAM J. Math. Anal.* **39**(1), 298–318 (2007).
34. G. R. Easley, D. Labate, and W.-Q. Lim, "Sparse directional image representations using the discrete shearlet transform," *Appl. Comput. Harmon. Anal.* **25**(1), 25–46 (2008).
35. G. Kutyniok and D. Labate, "Resolution of the wavefront set using continuous shearlets," *Trans. Am. Math. Soc.* **361**(5), 2719–2754 (2009).
36. S. Yi et al., "A shearlet approach to edge analysis and detection," *IEEE Trans. Image Process.* **18**(5), 929–941 (2009).
37. K. Guo, G. Kutyniok, and D. Labate, "Sparse multidimensional representations using anisotropic dilation and shear operators," in *Proc. Int. Conf. on the Interactions between Wavelets and Splines*, G. Chen and M. Lai, Eds., Athens, Georgia, pp. 189–201 (2005).
38. B. Vandeghinste et al., "Iterative CT reconstruction using shearlet-based regularization," *IEEE Trans. Nuclear Sci.* **60**(5), 3305–3317 (2013).
39. A. Pour Yazdanpanah, E. E. Regentova, and G. Bebis, "Algebraic iterative reconstruction-reprojection (AIRR) method for high performance sparse-view CT reconstruction," *Appl. Math. Inf. Sci.* **10**(6), 2007–2014 (2016).
40. K. Guo, D. Labate, and W.-Q. Lim, "Edge analysis and identification using the continuous shearlet transform," *Appl. Comput. Harmon. Anal.* **27**(1), 24–46 (2009).
41. B. Goossens et al., "Efficient design of a low redundant discrete shearlet transform," in *Proc. Int. Workshop Local and NonLocal Approximation in Image Processing* (2009).
42. I. Daubechies, *Ten Lectures on Wavelets*, SIAM, Philadelphia (1992).
43. T. Goldstein and S. Osher, "The split Bregman method for L1 regularized problems," *SIAM J. Imaging Sci.* **2**(2), 323–343 (2009).
44. S. Boyd et al., "Distributed optimization and statistical learning via the alternating direction method of multipliers," *Found. Trends Mach. Learn.* **3**(1), 1–122 (2011).
45. W. Yin et al., "Bregman iterative algorithms for L1-minimization with applications to compressed sensing," *SIAM J. Imaging Sci.* **1**, 143–168 (2008).
46. G. Kutyniok, M. Shahram, and X. Zhuang, "Shearlab: a rational design of a digital parabolic scaling algorithm," *SIAM J. Imaging Sci.* **5**, 1291–1332 (2012).

Biographies for the authors are not available.